RESEARCH ARTICLE

Three-Dimensional Trajectory–Speed–Energy Co-Optimization for XLUUVs Based on Feasible-Seed-Constrained Particle Swarm Optimization

Peng Bo[1,2], **Qingchang Guo**[2], **Liran Ma**[1,2] and **Jianbin Luo**[1,2,*]

[1] Department of Mechanical Engineering, Tsinghua University, Beijing 100084, China
[2] State Key Laboratory of Tribology in Advanced Equipment, Tsinghua University, Beijing 100084, China

Abstract

Long-range extra-large unmanned underwater vehicles (XLUUVs) require coordinated trajectory, speed, and hybrid energy management under spatially varying currents and operational constraints. This study develops a three-dimensional trajectory–speed–energy co-optimization framework using particle swarm optimization (PSO). Lateral trajectory points, segment-wise depths and speeds, and fuel cell power biases are jointly optimized within a mission-level current, propulsion, hydrogen-consumption, and battery state-of-charge (SOC) model. Sequential depth repair enforces the 100 m adjacent-segment depth-change limit, and feasibility-first selection coordinates the remaining operational constraints. In a 15,000 km analytical-current scenario, all ten complete co-optimization runs are feasible. Their mean hydrogen consumption is 23190.76 kg, a 30.34% reduction relative to the fixed-operation baseline, with a sample standard deviation of 700.81 kg. The sequential baseline achieves a 32.19% saving, and sensitivity studies show that the contributions of depth freedom, current-field adaptation, and power allocation depend on the tested environmental and energy-system conditions. These results quantify mission-level performance under the adopted discretized model.

Keywords: extra-large unmanned underwater vehicle (XLUUV), trajectory–speed–energy co-optimization, power allocation, particle swarm optimization (PSO).

1 Introduction

Long-endurance autonomous platforms must coordinate motion planning, propulsion demand, and onboard energy resources under spatially varying environmental conditions. For extra-large unmanned underwater vehicles (XLUUVs), ocean currents, operating depth, and navigation speed jointly determine hydrodynamic resistance and mission energy consumption; therefore, trajectory, speed, and energy management should be treated as coupled mission-level decisions.

Submitted: 30 September 2026
Revised: 10 November 2026
Accepted: 11 November 2026
Published: 27 November 2026

Vol. 1, **No.** 4, 2026.
10.62762/AEC.2026.456737

***Corresponding author:**
✉ Jianbin Luo
luojb@tsinghua.edu.cn

Citation
Bo, P., Guo, Q., Ma, L., & Luo, J. (2026). Three-Dimensional Trajectory–Speed–Energy Co-Optimization for XLUUVs Based on Feasible-Seed-Constrained Particle Swarm Optimization. *Aerospace Engineering Communications*, 1(4), 154–171.

© 2026 by the Authors. Published by Institute of Central Computation and Knowledge. This is an open access article under the CC BY license (https://creativecommons.org/licenses/by/4.0/).

Unmanned underwater vehicle (UUV) development has been driven by expanding mission requirements [1] and has moved from short-range observation platforms to long-endurance, long-range, and high-payload vehicles, with extra-large platforms now being procured [2]. A survey of autonomous underwater vehicle (AUV) technology [3] and a review of UUV energy technologies [4] identify energy supply and onboard autonomy as key limits on the operating envelope, and energy-optimized three-dimensional path planning has been pursued to extend AUV operational range [5]. At the mission level, the mission profile, vehicle motion, and energy-system constraints therefore have to be analyzed together rather than component by component.

For long-range missions, high-energy-density fuel cells combined with lithium batteries are a promising architecture [6–9]. Prior studies show that sizing, propulsion loading, and power-management policy must be coordinated: the fuel cell supplies sustained power, whereas the battery compensates load fluctuations and transient demands.

Ship energy-efficiency studies on combined speed–routing optimization [10], energy-efficiency measures [11], speed–trim control [12], route-segmented speed optimization with weather data [13], and multi-objective energy-efficiency optimization considering carbon tax [14] provide methodological evidence that route, speed, and operating-state decisions should be coordinated. However, these surface-vessel formulations do not directly represent the three-dimensional operating-depth freedom and hybrid-energy constraints of an XLUUV.

More directly, Wang and Li [15] used particle swarm optimization (PSO) to coordinate ship speed and fuel cell power under a prescribed route, but did not optimize lateral position or operating depth. Other studies similarly treat these decisions as separate layers: speed regulation is optimized for given routes and environmental conditions [16], path planning in current fields is handled with fast marching [17], A^* search [18], evolutionary algorithms [19], current-exploiting planners [20], and energy-aware feedback planning [21], and energy management is addressed through power-allocation strategies [22, 23], onboard energy storage [24, 25], and health-aware fuel cell operation [26, 27]. The remaining technical gap is therefore a unified XLUUV formulation in which three-dimensional trajectory, speed, and hybrid-energy decisions are optimized under common environmental, duration, power, SOC, and maneuverability constraints. This study addresses that gap with a feasible-seed-constrained PSO framework; the principal differences from [15] are summarized in Table 1.

Table 1. Comparison with Ref. [15].

Criterion	Ref. [15]	Present study
Research object	Fuel cell-powered ships	XLUUVs
Decision variables	Speed and fuel cell power	3D trajectory, speed, and fuel cell power
Environmental factors	Route and environmental conditions	3D nonuniform ocean current field
Optimization framework	Speed–energy co-optimization	3D trajectory–speed–energy co-optimization
Constraint handling	Not specified	Feasible-seed initialization and hierarchical constraint handling
Performance metrics	Hydrogen consumption and voyage time	Hydrogen consumption, voyage time, SOC, and constraint feasibility

However, directly transferring surface-vessel methods to UUVs involves a fundamental mismatch in optimization paradigms. Surface vessels operate primarily in a surface environment, whereas UUVs can select operating depths and adjust their trajectories in three dimensions. Their propulsion loads depend jointly on ground-referenced velocity, ocean current velocity, and vehicle attitude. Petres et al. [17] employed the fast marching method for underwater path planning, Garau et al. [18] used the A^* algorithm to search for paths in complex current fields, Alvarez et al. [19] applied evolutionary algorithms to AUV path planning in variable ocean environments, Witt and Dunbabin [20] proposed optimal path planning that exploits coastal currents, and Alam et al. [21] extended energy-aware feedback planning to long-range AUVs. These studies highlight the decisive role of environmental fields in trajectory selection. However, energy consumption in such approaches is generally represented by simplified cost functions related to speed or travel distance, with relatively limited consideration of energy-system constraints such as fuel cell efficiency characteristics, power ramp-rate limits, and battery state-of-charge (SOC)

safety bounds. Consequently, these approaches may not adequately capture the dynamic feasibility of hybrid energy systems.

At the hybrid energy system level, power allocation strategies have been extensively investigated. Tang and Wang [22] developed energy management strategies for hybrid power systems that account for the dynamic characteristics of the power sources. Zhou et al. [23] reviewed the architecture and power-management strategies of multi-stack fuel cell systems. Mutarraf et al. [24] reviewed energy storage systems for shipboard microgrids. Hou et al. [25] used hybrid energy storage to mitigate propulsion-load fluctuations in all-electric ships. A review of marine fuel cell technologies [26] and a degradation-adaptive energy management study for fuel cell hybrid electric vehicles [27] further demonstrate the need to jointly consider system efficiency, degradation state, and power allocation strategies. These studies show that power allocation directly affects fuel cell operating efficiency, energy storage safety, and load smoothing. However, if trajectory and speed decisions cause propulsion loads to remain in an unfavorable operating range over extended periods, even sophisticated power allocation can only provide local adjustments under the imposed load profile. Therefore, energy optimization for long-range XLUUV missions should not be limited to power allocation under a prescribed propulsion load. Instead, trajectory and speed decisions should also be exploited to actively regulate propulsion demand and reduce energy consumption at the mission level.

For long-range XLUUV missions, trajectory and depth determine the encountered current and relative flow velocity; speed determines duration and propulsion demand; and fuel cell power allocation governs battery SOC evolution and downstream feasibility. A sequential design fixes upstream decisions before their energy consequences are known and can therefore provide only local compensation under the resulting load profile.

The work makes three contributions to this cross-layer problem. A mission-level model is formulated in which lateral trajectory points, segment depths and speeds, and fuel cell power biases share one set of environmental and operational constraints. A feasible-seed-constrained PSO strategy is then built from economical-speed and favorable-current priors, sequential depth repair, hierarchical power/SOC projection, and feasibility-first selection. Finally, progressive cases, a sequential A^* baseline, component ablations, and paired sensitivity studies are used to measure the attainable savings and to identify the environmental and energy-system conditions under which trajectory, depth, and power-allocation freedoms remain useful.

2 Research Object and System Modeling

2.1 Geometric Parameters and Operating Environment of the XLUUV

To describe the XLUUV's navigation state in three-dimensional mission space and its interaction with the ocean current environment, a fixed coordinate frame O-XYZ is adopted to represent the trajectory and current field, while a body-fixed coordinate frame o_b-$x_b y_b z_b$ is used to describe its motion directions. The fixed frame characterizes the vehicle's position relative to the ground and the spatial distribution of ocean currents, whereas the body-fixed frame describes the vehicle's velocity direction and attitude. These coordinate frames are illustrated in Figure 1.

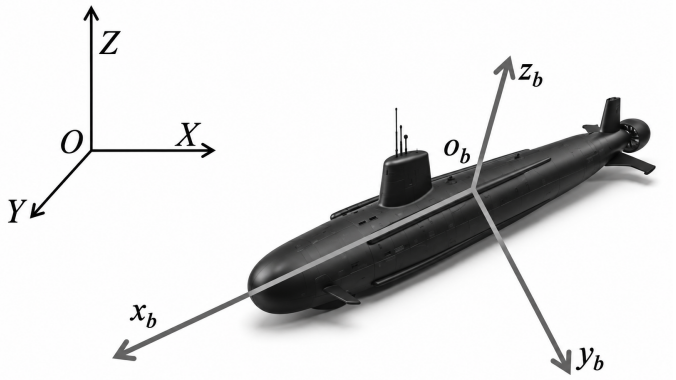


Figure 1. Schematic of the inertial and body-fixed coordinate systems of the XLUUV.

In the fixed coordinate frame, the ground-velocity vector of the XLUUV, the ocean-current velocity vector, and the velocity vector relative to the surrounding water are denoted by $\mathbf{v}_\mathrm{g}$, $\mathbf{u}_\mathrm{c}$, and $\mathbf{v}_\mathrm{r}$, respectively. These vectors satisfy the following relationship:

$$\mathbf{v}_\mathrm{r} = \mathbf{v}_\mathrm{g} - \mathbf{u}_\mathrm{c}, \tag{1}$$

where the units of $\mathbf{v}_\mathrm{g}$, $\mathbf{u}_\mathrm{c}$, and $\mathbf{v}_\mathrm{r}$ are all $\mathrm{m/s}$. The magnitude and direction of the relative water velocity jointly determine the primary hydrodynamic forces acting on the vehicle and, consequently, affect its propulsion power demand. Therefore, mission-level decision variables, such as trajectory position, operating depth, and speed, can modify the relative flow velocity through local ocean currents, thereby influencing energy consumption. Throughout

this paper, bold lowercase letters are used to denote vectors, whereas italic lowercase letters represent the corresponding scalar magnitudes. In particular, v_r denotes the magnitude of the relative water velocity.

The vehicle considered in this study is a torpedo-shaped XLUUV, with a length of $L_{\mathrm{v}} = 70$ m and a maximum diameter of $D = 5.2$ m. These parameters are used to establish a consistent basis for trajectory planning, propulsion load estimation, and energy consumption calculation. Since this study focuses on the relative energy performance of different decision-making strategies in long-range missions, the vehicle's motion is simplified appropriately at the mission-level optimization layer. Specifically, the low-level navigation control system is assumed to align the vehicle's ground-velocity direction with the tangential direction of the planned trajectory segment. Sideslip and high-frequency transient effects during turning are neglected, and the average speed of each segment is used to characterize steady-state cruising.

Under these assumptions, local current, relative water velocity, and trajectory geometry define the propulsion-load and energy-consumption mapping used to compare decision-making strategies. The speed, depth, adjacent-depth-change, and heading constraints are listed in Table 2.

Table 2. Velocity and depth constraint parameters.

Parameter	Symbol	Value	Unit
Minimum speed	$v_{\min}$	1.0	m/s
Maximum speed	$v_{\max}$	2.5	m/s
Minimum operating depth	$z_{\min}$	100	m
Maximum operating depth	$z_{\max}$	1000	m
Maximum depth change between adjacent segments	$\Delta z_{\max}$	100	m
Maximum heading change	$\Delta\psi_{\max}$	30	°

2.2 Fuel Cell–Lithium Battery Hybrid Energy System Architecture

To meet the requirements of XLUUV long-range missions for high energy density and power-regulation capability, a fuel cell–lithium battery hybrid energy system is adopted in this study. The system primarily consists of a hydrogen fuel cell, a lithium battery pack, a unidirectional DC/DC converter, a bidirectional DC/DC converter, a DC bus, and propulsion and auxiliary loads, as illustrated in Figure 2. The fuel cell primarily supplies the average power demand, while the lithium battery compensates for load fluctuations through bidirectional power regulation and maintains the SOC within the allowable range.

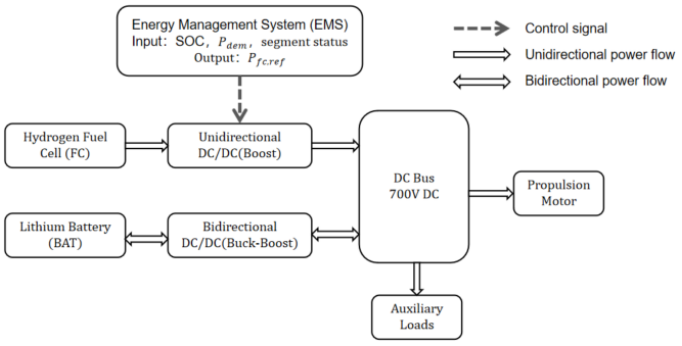


Figure 2. Architecture of the fuel cell-lithium battery hybrid energy system.

The total power demand on the DC bus is then given by

$$P_{\mathrm{dem}}(t) = P_{\mathrm{prop}}(t) + P_{\mathrm{aux}}(t) = P_{\mathrm{fc}}(t) + P_{\mathrm{bat}}(t), \quad (2)$$

where $P_{\mathrm{dem}}(t)$ denotes the total system power demand, $P_{\mathrm{prop}}(t)$ is the propulsion system power, $P_{\mathrm{aux}}(t)$ represents the power consumed by navigation, control, and other auxiliary equipment, $P_{\mathrm{fc}}(t)$ is the fuel cell output power, and $P_{\mathrm{bat}}(t)$ denotes the battery-side power. In this paper, $P_{\mathrm{fc}}(t)$ is defined as positive. Accordingly, the battery power can be determined from the power balance as follows:

$$P_{\mathrm{bat}}(t) = P_{\mathrm{dem}}(t) - P_{\mathrm{fc}}(t). \quad (3)$$

Accordingly, when $P_{\mathrm{bat}}(t) > 0$, the lithium battery discharges power to the DC bus. When $P_{\mathrm{bat}}(t) < 0$, the fuel cell supplies the load demand while charging the lithium battery. The fuel cell output power is constrained by its rated operating range, i.e.,

$$P_{\mathrm{fc,min}} \le P_{\mathrm{fc}}(t) \le P_{\mathrm{fc,max}}, \quad (4)$$

where $P_{\mathrm{fc,min}}$ and $P_{\mathrm{fc,max}}$ denote the minimum and maximum allowable fuel cell output powers, respectively, to prevent the fuel cell from operating for extended periods in an inefficient low-power region or an overloaded region. The battery SOC is defined to satisfy the following constraints:

$$SOC_{\min} \le SOC(t) \le SOC_{\max}, \quad (5)$$

where $SOC_{\min}$ and $SOC_{\max}$ denote the minimum and maximum allowable battery state-of-charge limits, respectively. The detailed dynamic evolution of the SOC is calculated in the subsequent energy consumption model according to the battery's charging and discharging states.

For adjacent segments, define $\Delta P_{\mathrm{fc},i} = |P_{\mathrm{fc},i} - P_{\mathrm{fc},i-1}|$, $\Delta P_{\mathrm{fc,max}} = \max_{i\geq 2} \Delta P_{\mathrm{fc},i}$, and $S_{\mathrm{fc}} = \sum_{i=2}^{N} \Delta P_{\mathrm{fc},i}$. These command-step metrics, expressed in kW, characterize the segment-wise fuel cell power sequence. Battery energy throughput is $E_{\mathrm{thr}} = \sum_i |P_{\mathrm{bat},i}|\Delta t_i/1000$ MWh. The feasibility set comprises fuel cell power bounds, SOC bounds, terminal SOC recovery, and the segment-wise SOC-derived battery-power interval.

3 Hydrodynamic and Energy Consumption Models

3.1 Relative Water Velocity and Propulsion Power

In a nonuniform ocean current field, the hydrodynamic resistance experienced by the XLUUV is determined by its velocity relative to the surrounding water. Let the ground-velocity vector and the local ocean-current velocity vector of the i-th trajectory segment be denoted by $\mathbf{v}_{g,i}$ and $\mathbf{u}_{c,i}$, respectively. The magnitude of the relative water velocity is then defined as follows:

$$v_{r,i} = \left\| \mathbf{v}_{g,i} - \mathbf{u}_{c,i} \right\|_2 , \tag{6}$$

where $v_{r,i}$ is measured in m/s.

Under the motion assumptions, trajectory geometry and the optimized segment speed determine ground velocity, while the current enters through the ground–current vector difference in (6).

The implemented mission-level propulsion model uses a single effective resistance–propulsion coefficient. For segment i,

$$P_{\mathrm{prop},i} = \kappa_{\mathrm{prop}} v_{r,i}^3 f_{\psi,i} f_{z,i} f_{d,i}, \tag{7}$$

where $\kappa_{\mathrm{prop}} = 27.5\ \mathrm{kW/(m\,s^{-1})^3}$, $f_{\psi,i} = 1 + k_\psi|\Delta\psi_i|$, $f_{z,i} = 1 + k_z|\Delta z_i|$ with $\Delta z_i = z_i - z_{i-1}$, and $f_{d,i}$ is the depth-operating sensitivity factor, equal to unity in the nominal model. The coefficient corresponds to $\kappa_{\mathrm{prop}} = \rho C_D A/(2\eta_p)$ [28], with streamlined-hull geometry and resistance reference data available from the DARPA SUBOFF program [29, 30], and the numerical model identifies only this combined coefficient. The reference area A and drag coefficient C_D are therefore not separately identified, and κ_{prop} is treated as a lumped effective mission-level coefficient rather than a hull-only drag estimate. Let L_i denote the segment length and $v_{g,i}$ the ground-speed magnitude. The travel time is

$$\Delta t_i = \frac{L_i}{v_{g,i}}. \tag{8}$$

The propulsion power $P_{\mathrm{prop},i}$ is determined by the relative water speed $v_{r,i}$, whereas Δt_i is determined by the ground speed $v_{g,i}$. Consequently, trajectory choices affect both propulsion power and mission duration.

3.2 Hydrogen Consumption and SOC Evolution

Let $\mathrm{LHV}_{\mathrm{H_2}}$ denote the lower heating value of hydrogen and $\eta_{\mathrm{fc}}(P_{\mathrm{fc}})$ the fuel cell efficiency. The instantaneous hydrogen consumption rate in the i-th trajectory segment, denoted by $\dot{m}_{\mathrm{H_2}}$, is determined by the fuel cell output power and its corresponding efficiency, as follows:

$$\dot{m}_{\mathrm{H_2}}(t) = \frac{P_{\mathrm{fc}}(t)}{\eta_{\mathrm{fc}}(P_{\mathrm{fc}})\,\mathrm{LHV}_{\mathrm{H_2}}}. \tag{9}$$

By summing the hydrogen consumption over all trajectory segments, the total hydrogen consumption over the entire mission is obtained as follows:

$$m_{\mathrm{H_2,total}} = \sum_{i=1}^{N} \dot{m}_{\mathrm{H_2},i}\,\Delta t_i, \tag{10}$$

where N denotes the total number of trajectory segments. The battery SOC is updated separately according to the charging and discharging states. In this study, $P_{\mathrm{bat},i} > 0$ indicates discharging, whereas $P_{\mathrm{bat},i} < 0$ indicates charging. Let $E_{\mathrm{bat}} = 8$ MWh denote the nominal battery energy capacity. The SOC bounds define the admissible fraction of this nominal capacity. Let η_{dis} and η_{ch} denote the discharging and charging efficiencies. In the numerical update, $P_{\mathrm{bat},i}$ is in kW and Δt_i is in hours, so E_{bat} is converted to kWh. The SOC at the beginning of the $(i+1)$-th trajectory segment is

$$SOC_{i+1} = \begin{cases} SOC_i - \dfrac{P_{\mathrm{bat},i}\Delta t_i}{E_{\mathrm{bat}}\eta_{\mathrm{dis}}}, & P_{\mathrm{bat},i} > 0, \\ SOC_i - \dfrac{P_{\mathrm{bat},i}\eta_{\mathrm{ch}}\Delta t_i}{E_{\mathrm{bat}}}, & P_{\mathrm{bat},i} < 0. \end{cases} \tag{11}$$

Because battery discharging power is defined as positive and charging power as negative in this study, discharging decreases the SOC, whereas charging increases it. Furthermore, to preserve sufficient energy reserves for recovery or emergency operations at the end of the mission, a terminal SOC restoration requirement is imposed during optimization.

4 Trajectory–Speed–Energy Co-Optimization Model

4.1 Segment-Wise Trajectory Representation

For long-range XLUUV missions, the planned trajectory is discretized along the x-direction into

N segments. The three-dimensional trajectory is represented using a set of trajectory nodes and a set of trajectory segments, defined as follows:

$$\mathbf{P} = \{\mathbf{P}_0, \mathbf{P}_1, \ldots, \mathbf{P}_N\}, \tag{12}$$

where the i-th trajectory control point is denoted by $\mathbf{P}_i$. To enable the joint optimization of trajectory, speed, and energy state, each trajectory segment is characterized by its spatial position, speed, average operating depth, and fuel cell power bias:

$$\Gamma_i = (\mathbf{P}_{i-1}, \mathbf{P}_i, v_i, \bar{z}_i, \delta P_{\mathrm{fc},i}), \quad i = 1, 2, \ldots, N, \tag{13}$$

where v_i denotes the speed of the i-th trajectory segment, and $\delta P_{\mathrm{fc},i}$ is the fuel cell power bias variable. The average operating depth is defined as $\bar{z}_i$. Since a segment-wise average steady-state model is adopted to characterize propulsion loads and energy consumption, the local ocean current parameters are retrieved based on the average operating depth. To ensure that the optimized trajectory satisfies the maneuverability constraints of the XLUUV, the horizontal heading angle of each trajectory segment is calculated. Let ψ_i denote the heading angle of the i-th segment. The heading change between two adjacent segments is then given by $\Delta\psi_i$, which must satisfy the following constraint:

$$|\Delta\psi_i| \le \Delta\psi_{\max}. \tag{14}$$

4.2 Optimization Variables and Objective Function

The trajectory is discretized at equal intervals along the x-direction, i.e., $x_i = x_0 + i \cdot \Delta x,\ i = 0, 1, \cdots, N$. The horizontal positions of the starting and ending points are determined by the mission boundary conditions, while the internal lateral trajectory control points y_i and the operating depths of individual segments z_i are treated as spatial decision variables. Together with the segment-wise speeds and fuel cell power biases, the decision vector of particle j is defined as follows:

$$\begin{aligned}\mathbf{x}_j = [&y_1, \ldots, y_{N-1}, z_1, \ldots, z_N, v_1, \ldots, v_N,\\ &\delta P_{\mathrm{fc},1}, \ldots, \delta P_{\mathrm{fc},N}],\end{aligned} \tag{15}$$

where y_i is used to adjust the lateral spatial position of the trajectory, z_i controls the operating depth of each trajectory segment, v_i denotes the speed of the i-th segment, and $\delta P_{\mathrm{fc},i}$ represents the fuel cell power bias. Therefore, the dimension of the optimization vector is $4N - 1$.

The primary objective is to minimize the total mission hydrogen consumption over the set $\mathcal{F}$ of solutions satisfying all prescribed operational constraints:

$$\min_{\mathbf{x}_j \in \mathcal{F}} \quad m_{\mathrm{H_2,total}}(\mathbf{x}_j). \tag{16}$$

Here $\mathcal{F}$ includes speed and depth bounds, the adjacent-segment depth-change and horizontal-turn limits, mission duration, fuel cell power bounds, both SOC safety bounds, and terminal SOC recovery.

5 Feasible-Seed-Constrained PSO Solution Strategy

5.1 Particle Swarm Updates, Power Allocation, and Constraint Projection

For the established three-dimensional trajectory–speed–energy co-optimization problem of the XLUUV, the decision variables include trajectory control points, segment-wise speeds, operating depths, and fuel cell power biases. As the number of trajectory segments increases, the dimensionality of the optimization problem also increases. Therefore, to improve the coverage of potentially low-energy-consumption and feasible regions by the initial population, three types of prior information are introduced in addition to random initialization and are combined in one composite seed particle: an economical-speed prior, a favorable-current-corridor trajectory prior, and a depth-corridor prior.

Economical-speed seed: Based on the hull resistance characteristics and the fuel cell efficiency–power characteristics, a reference economical speed v_{eco}, corresponding to relatively low energy consumption per unit distance, is determined in advance. The speeds of individual trajectory segments are then initialized around this reference value, thereby providing the particle swarm with an initial search region characterized by a low-energy-consumption speed distribution.

Favorable-current-corridor trajectory seed: Based on the spatial distribution of the prescribed ocean current field, the directions and magnitudes of ocean currents at different locations are analyzed. A sequence of trajectory control points is generated along the dominant local current directions, such that the vehicle's direction of travel is aligned as closely as possible with the local current direction. This helps reduce the relative water velocity and the associated propulsion resistance under a given ground-speed condition.

Depth-corridor seed: The nominal sequence is $z_i^{\mathrm{seed}} = 520 + 170\sin(2\pi x_i^{\mathrm{mid}}/L_{\mathrm{M}} + 0.7)$ m and is repaired using

the operator below, where $L_{\mathrm{M}} = 15000$ km is the mission length and x_i^{mid} is the midpoint of the i-th segment along x. A composite particle combines this depth sequence, the favorable-current lateral sequence, a speed of 3.65 kn, and zero fuel cell bias; the other particles are initialized uniformly within their search bounds. Cases B–D use the corresponding restricted composite seed.

The three priors provide information on speed, horizontal trajectory, and operating depth and are combined in the composite particle, while all other particles are randomly initialized. Subsequent PSO updates retain the full decision-space bounds.

After constructing the initial population, the standard PSO algorithm is employed for iterative search. Let $\mathbf{V}_j^k$ denote the search-step (velocity) vector of the j-th particle at the k-th PSO iteration. The particle velocity and position are updated according to the following equations, which follow the original PSO formulation [31] with an inertia weight, and whose stability and convergence behavior are analyzed in [32]:

$$\begin{aligned}\mathbf{V}_j^{k+1} =& \omega \mathbf{V}_j^k + c_1 r_1 \left(\mathbf{B}_j^k - \mathbf{X}_j^k\right) \\ &+ c_2 r_2 \left(\mathbf{G}^k - \mathbf{X}_j^k\right),\end{aligned} \tag{17}$$

$$\mathbf{X}_j^{k+1} = \mathbf{X}_j^k + \mathbf{V}_j^{k+1}, \tag{18}$$

where ω denotes the inertia weight at the k-th iteration, c_1 and c_2 represent the individual cognitive coefficient and social learning coefficient, respectively, and r_1 and r_2 are independently generated random numbers uniformly distributed over the interval $[0, 1]$. $\mathbf{X}_j^k$ and $\mathbf{V}_j^k$ denote the decision vector and search-step vector of the j-th particle at the k-th iteration, respectively, both of which have a dimension of $4N - 1$. $\mathbf{B}_j^k$ represents the personal-best position attained by the j-th particle up to the k-th iteration, whereas $\mathbf{G}^k$ denotes the global-best position of the entire swarm. After boundary clipping and before environmental or energy evaluation, the depth sequence is repaired in forward segment order. Starting from the prescribed initial depth $z_0^{\mathrm{rep}} = 300$ m, define

$$\begin{aligned} l_i &= \max(z_{\mathrm{search,min}}, z_{i-1}^{\mathrm{rep}} - 100), \\ u_i &= \min(z_{\mathrm{search,max}}, z_{i-1}^{\mathrm{rep}} + 100), \\ z_i^{\mathrm{rep}} &= \min\{u_i, \max(l_i, z_i^{\mathrm{raw}})\}. \end{aligned}$$

The search bounds are $z_{\mathrm{search,min}} = 150$ m and $z_{\mathrm{search,max}} = 900$ m, a conservative subset of the physical operating interval in Table 2. Since the preceding repaired depth lies within these bounds, $[l_i, u_i]$ is nonempty. Induction therefore guarantees both the depth bounds and $|z_i^{\mathrm{rep}} - z_{i-1}^{\mathrm{rep}}| \le 100$ m, including the first transition from the initial depth. This order-dependent $O(N)$ sequential interval projection writes repaired depths back to the particle coordinates before personal/global-best updates; currents, geometry, propulsion power, and SOC are then recomputed. Horizontal turning enters the feasibility-first ranking together with the remaining constraints.

Regarding energy management, the candidate fuel cell output power is determined based on the power demand of the current trajectory segment and adjusted according to the current battery SOC and the fuel cell power bias included in the optimization variables. The candidate fuel cell output power for the i-th trajectory segment is defined as follows:

$$P_{\mathrm{fc},i}^{\mathrm{raw}} = P_{\mathrm{dem},i} + k_{\mathrm{SOC}}(SOC_0 - SOC_i) + \delta P_{\mathrm{fc},i}, \tag{19}$$

where $P_{\mathrm{dem},i}$ denotes the segment demand, and $k_{\mathrm{SOC}} = 240$ kW per unit SOC. The bias is implemented as $\delta P_{\mathrm{fc},i} = 18\epsilon_i$ kW with $\epsilon_i \in [-1, 1]$, hence $\delta P_{\mathrm{fc},i} \in [-18, 18]$ kW. When $SOC_i < SOC_0$, the feedback term increases the candidate fuel cell power; when $SOC_i > SOC_0$, it reduces the candidate power.

The candidate fuel cell power is mapped to the allowable power range to obtain the actual fuel cell output power:

$$P_{\mathrm{fc},i} = \Pi_c\left(P_{\mathrm{fc},i}^{\mathrm{raw}}\right), \tag{20}$$

where $\Pi_c(\cdot)$ denotes the fuel cell power constraint projection operator, which maps the candidate power to the allowable fuel cell output power range. If $P_{\mathrm{fc},i}^{\mathrm{raw}}$ lies within the prescribed power limits, then $P_{\mathrm{fc},i} = P_{\mathrm{fc},i}^{\mathrm{raw}}$. Otherwise, it is projected onto the corresponding power boundary.

After the initial fuel cell power saturation, $P_{\mathrm{bat},i}$ is obtained from the DC-bus power balance. To keep the next segment-end SOC within its admissible interval, the energy-available limits for the current segment are

$$\begin{aligned} P_{\mathrm{dis},i}^{SOC} &= \frac{(SOC_i - SOC_{\min})E_{\mathrm{bat}}\eta_{\mathrm{dis}}}{\Delta t_i}, \\ P_{\mathrm{ch},i}^{SOC} &= \frac{(SOC_{\max} - SOC_i)E_{\mathrm{bat}}}{\eta_{\mathrm{ch}}\Delta t_i}, \end{aligned}$$

and the projection requires $-P_{\mathrm{ch},i}^{SOC} \le P_{\mathrm{bat},i} \le P_{\mathrm{dis},i}^{SOC}$ together with the fuel cell operating bounds. These segment-specific limits follow from the SOC energy balance and are not independent battery nameplate power ratings.

Algorithm 1: Feasible-Seed-Constrained PSO Algorithm with Hierarchical Projection for Co-Optimization

Input: Ocean current field data, mission start/end points, number of trajectory segments N, swarm size M, maximum number of iterations $K_{\max}$, XLUUV geometric parameters, energy system parameters, and constraint parameters.

Output: Optimized three-dimensional trajectory, speed sequence, fuel cell power sequence, SOC trajectory, and optimal decision vector $\mathbf{G}^*$.

Generate the initial population consisting of randomly initialized particles and one composite particle combining the economical-speed, favorable-current-corridor, and depth-corridor priors;

Perform variable boundary handling and initial energy-state feasibility checks, and calculate the initial personal best and global best;

for $k = 0, \ldots, K_{\max} - 1$ **do**

  Update particle search-step vectors according to (17), and update particle positions according to (18);

  Clip variable bounds, apply the sequential depth repair, and write repaired depths back to the particle;

  Reconstruct the trajectory and calculate the local ocean current parameters according to the updated decision vectors, including the heading, operating depth, and local current parameters;

  Calculate the relative water velocity, propulsion power, travel time, and total power demand according to (6), (7), (8), and (2);

  Calculate the candidate fuel cell output power $P_{\mathrm{fc},i}^{\mathrm{raw}}$ according to (19), and perform fuel cell power-boundary projection according to (20);

  Calculate the battery power according to the power balance, and check the SOC feasibility according to the hierarchical projection strategy. If necessary, further adjust the actual fuel cell output power;

  Update the total hydrogen consumption and SOC state according to (9)–(11);

  Audit candidate feasibility, evaluate the objective (16), and calculate the normalized residual constraint violation;

  Update personal and global bests by feasibility first: feasible dominates infeasible; among feasible solutions minimize hydrogen consumption; among infeasible solutions minimize violation;

  if *the maximum number of iterations is reached or a predefined stopping criterion is satisfied* **then**

    break;

  end

end

Evaluate the final solution against the complete constraint set and record its trajectory, energy performance, feasibility status, and constraint residuals;

5.2 Analytical Ocean-Current Field and Evaluation Procedure

The analytical field defined in Table 3 is used throughout the comparative and sensitivity studies so that all strategies are evaluated under a common, reproducible environmental model and constraint audit.

Algorithm 1 summarizes the trajectory, power/SOC, feasibility-audit, and best-update sequence.

6 Simulation Experiments and Results Discussion

6.1 Simulation Scenario and Parameters

To evaluate the proposed trajectory–speed–energy co-optimization method, a three-dimensional mission-level scenario is constructed with a projected length of 15,000 km along the x-direction. The y-axis represents lateral displacement and the z-axis represents depth. Its analytical current field provides controlled favorable-current, adverse-current, and vertically varying regions for quantifying the effects of the decision variables on mission energy consumption.

The analytical current field combines a favorable-current corridor, an adverse-current region, and a sinusoidal background current. The favorable-current corridor and the adverse-current region have Gaussian lateral and depth profiles. The depth center of the favorable corridor varies along track with amplitude A_z, while the Gaussian depth dependence remains present for every tested amplitude. Table 3 summarizes the implemented field.

Table 3. Analytical ocean-current field used in the reproducible simulation.

Quantity	Definition (coordinates x, y in km; depth z in m)
Current vector	Nominally $\mathbf{u}_c = [u_x, 0, 0]^{\mathsf{T}}$; direction is perturbed in the environmental-variation study
Along-track component	$u_x = a[u_{\mathrm{fav}} - u_{\mathrm{adv}} + 0.04\sin(4\pi x/L_{\mathrm{M}})]$
Favorable current	$u_{\mathrm{fav}} = 0.42\exp[-(y - y_c(x))^2/(2\cdot 75^2) - (z - z_c(x))^2/(2\cdot 190^2)]$
Lateral corridor center	$y_c(x) = 95\sin(2\pi x/L_{\mathrm{M}}) + 45\sin(6\pi x/L_{\mathrm{M}})$
Depth corridor center	$z_c(x) = 520 + A_z\sin(2\pi x/L_{\mathrm{M}} + 0.7)$
Adverse current	$u_{\mathrm{adv}} = 0.13\exp[-(y + 105)^2/(2\cdot 95^2) - (z - 260)^2/(2\cdot 150^2)]$
Current scale, vertical amplitude, and mission length	$a = 1$; $A_z = 170$ m nominally and $A_z \in \{0, 170, 340\}$ m in sensitivity checks; $L_{\mathrm{M}} = 15000$ km

Table 4. Main Case A–F experiment under the same 15,000 km mission and common duration upper bound. B–F use ten common seeds; A is deterministic. SD denotes sample standard deviation, RSD denotes relative standard deviation; saving is relative to Case A.

Case	Mean H_2 / kg	SD / kg	RSD / %	Saving / %	Time / h	Terminal SOC	Minimum SOC	Fully feasible
A	33289.40	—	—	0.00	1928.42	0.600	0.600	1/1
B	27725.13	48.36	0.174	16.71	2227.24	0.589	0.423	10/10
C	25751.31	36.78	0.143	22.64	2230.07	0.600	0.600	10/10
D	26104.61	17.65	0.068	21.58	2223.10	0.594	0.561	10/10
E	23190.76	700.81	3.022	30.34	2227.15	0.583	0.325	10/10
F	22574.20	228.84	1.014	32.19	2227.44	0.594	0.342	10/10

The implementation uses $N = 24$ equal along-track intervals, $\Delta x = 625$ km, an initial depth of 300 m, and nominal vertical-center amplitude $A_z = 170$ m. The lateral search bounds are $[-180, 180]$ km; speed proposals are searched within $[3.2, 5.8]$ kn, while the final audit enforces the physical interval $[1.0, 2.5]\,\mathrm{m\,s^{-1}}$ in Table 2. The normalized fuel cell bias lies in $[-1, 1]$ and is multiplied by 18 kW. The PSO uses 50 particles and 120 iterations (6000 objective evaluations per run), with $c_1 = c_2 = 1.55$, inertia decreasing from approximately 0.82 to 0.38, and coordinate-wise search-step clipping at 18% of each search span. The time reference is $T_0 = L_{\mathrm{M}}/(3.65 \times 1.852) = 2219.0006$ h; the operational audit limit is explicitly $T_{\max} = 1.005\ T_0 = 2230.0956$ h, retaining a 0.5% mission allowance. This allowance is not a floating-point tolerance. The battery capacity is 8 MWh, charge/discharge efficiencies are 0.92/0.94, auxiliary power is 62 kW, and fuel cell bounds are 160–640 kW. The same physical model and audit rules apply to all cases.

6.2 Comparative Case Setup

Six cases isolate the effects of successive decision freedoms. Cases A–E progress from fixed operation to three-dimensional co-optimization, whereas Case F provides a sequential A^* path-planning baseline followed by fixed-route operating-state optimization.

All cases share the mission, current field, physical model, and constraint definitions. Means, sample standard deviations, RSDs, and saving rates are calculated from the ten runs of each stochastic case. Case A is deterministic and is evaluated once. Horizontal start/end positions are fixed.

Case A: Fixed-Operation Baseline. A straight-line trajectory, fixed reference speed, and rule-based power allocation establish the full-mission reference. The fuel cell follows instantaneous demand within its operating range, after which SOC-feasibility projection determines the battery contribution.

Case B: Speed–Power Co-Optimization under a Fixed

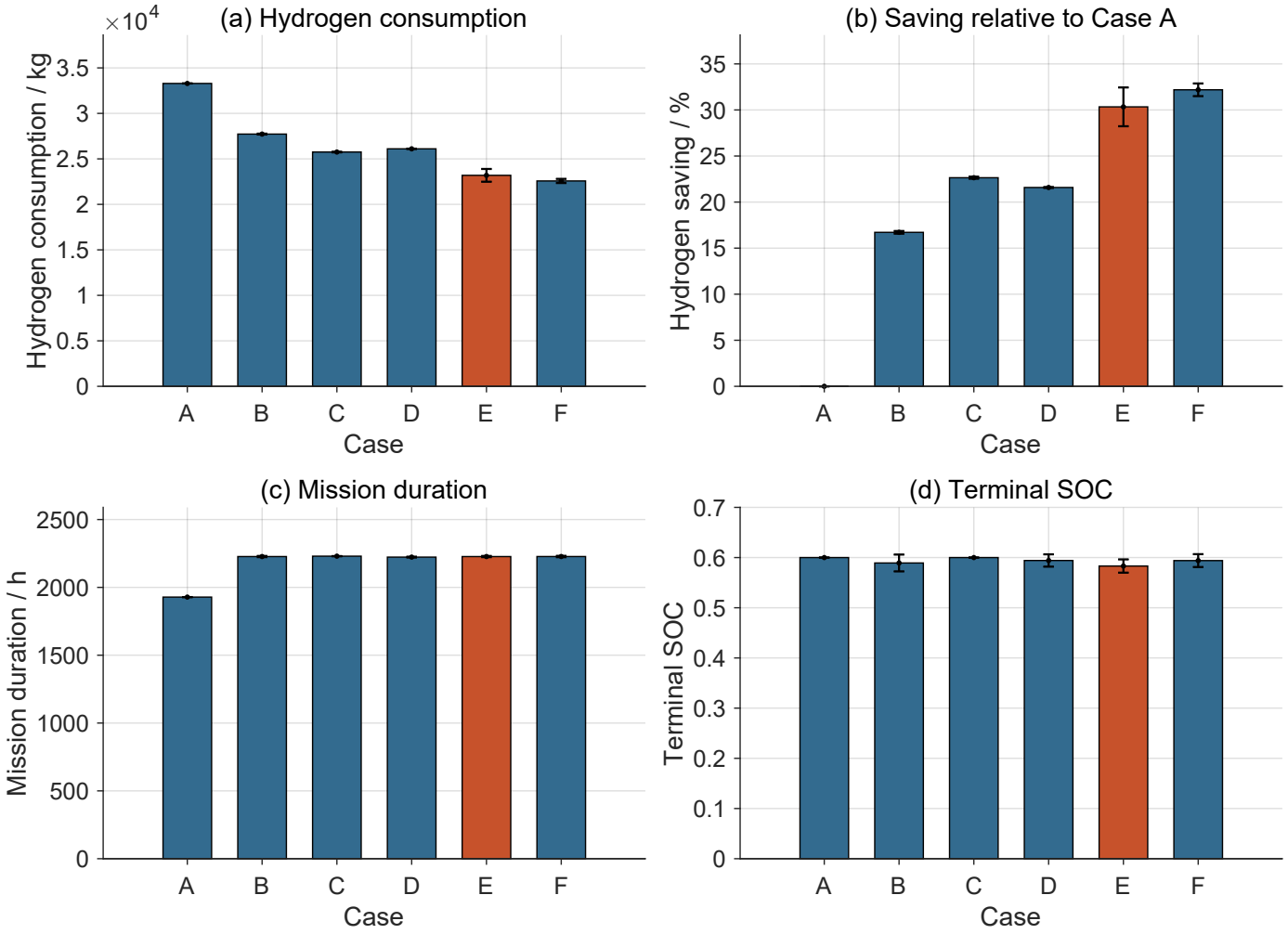


Figure 3. Results for Cases A–F: (a) hydrogen consumption, (b) saving relative to Case A, (c) mission duration, and (d) terminal SOC. B–F: $n = 10$, error bars denote sample standard deviations; A is deterministic.

Trajectory. PSO optimizes segment speeds and fuel cell biases while retaining the straight route, thereby isolating speed–power coordination.

Case C: Two-Dimensional Trajectory–Speed Joint Optimization. PSO optimizes lateral nodes and segment speeds, while power allocation remains rule based as in Case A. The A/C comparison evaluates two-dimensional motion optimization without an optimized energy-allocation variable.

Case D: Two-Dimensional Trajectory–Speed–Energy Co-Optimization. Lateral nodes, segment speeds, and fuel cell biases are jointly optimized. The C/D and B/D comparisons isolate optimized power allocation and lateral trajectory freedom, respectively.

Case E: Three-Dimensional Trajectory–Speed–Energy Co-Optimization. Case E adds segment depth to the Case D decision space; all other settings are retained so that D/E isolates vertical spatial selection.

Case F: Sequential A^* Baseline. Current-aware A^* first produces a low-propulsion-energy spatial path. The path is then fixed while the same speed–fuel cell optimization and energy-state calculation used in Case B are applied. The E/F comparison therefore contrasts unified and staged decision making.

6.3 Simulation Results and Discussion

Table 4 and Figure 3 report the comparison for Cases A–F. All cases cover the same 15,000 km mission and satisfy the common duration upper bound $T_{\max} = 2230.0956$ h. Thus, the savings are duration-constrained mission-energy comparisons, and an optimized case may use more of the admissible time to reduce propulsion demand. All ten runs of each stochastic case pass every prescribed constraint. Case A consumes 33289.40 kg of hydrogen.

Case B achieves a mean consumption of 27725.13 kg, a saving of 16.71% relative to Case A. Case C, which combines lateral trajectory and speed optimization with rule-based power allocation, achieves 25751.31 kg

and 22.64% savings. Its sample standard deviation is 36.78 kg and its RSD is 0.143%.

Case D introduces fuel cell bias variables in addition to lateral trajectory and speed. The paired difference $m_{\mathrm{H}_2,D} - m_{\mathrm{H}_2,C}$ has a mean of 353.30 kg and a sample standard deviation of 39.48 kg; its paired Student-t 95% confidence interval is $[325.06, 381.55]$ kg. All ten differences are positive, so Case D has higher hydrogen consumption than Case C under the adopted optimization budget.

The complete three-dimensional scheme, Case E, yields a mean hydrogen consumption of 23190.76 kg, a sample standard deviation of 700.81 kg, and an RSD of 3.022%. Its saving relative to Case A is 30.34%. Mean consumption is 11.16% below Case D. The median, minimum, and maximum consumptions are 23187.84, 22230.69, and 24232.85 kg, respectively. Across these runs, the largest adjacent-segment depth change is 100.000 m and the maximum depth-change violation is zero. These findings support feasible model-level performance for the nominal scenario, but they do not imply that depth freedom is intrinsically beneficial under every environmental or power-system condition.

Case F uses a current-aware layered shortest-path search followed by fixed-route speed–power optimization. The route stage evaluates propulsion costs with ground speed and current both expressed in m/s. It is implemented as a layered shortest-path recursion, equivalent to zero-heuristic A^* on this acyclic route graph. The route grid uses lateral points from -180 to 180 km in 30 km increments and depths from 150 to 900 m in 50 m increments. Each edge advances one segment and changes at most one lateral grid index and two depth indices. Both terminal lateral offset and terminal depth are fixed at 0 km and 300 m. Under the same downstream optimizer and full audit, all ten runs are feasible. Its mean hydrogen consumption is 22574.20 kg, with a sample standard deviation of 228.84 kg and an RSD of 1.014%; the saving relative to Case A is 32.19%. Case E consumes 616.56 kg more on average, or 2.73% relative to Case F.

The representative Case E solution consumes 23205.58 kg hydrogen. Figures 4 and 5 show its trajectory, depth-step sequence, power allocation, and SOC evolution; the complete independent constraint audit in Table 5 confirms feasibility within the declared numerical tolerance.

The gains from the individual decision freedoms do not add up linearly; they depend on the operating condition. Depth freedom is the clearest example. Whether it pays off depends on the vertical current structure that can be exploited, on the added difficulty of handling depth constraints, and on the larger search space, so it has to be judged by the resulting energy use and feasibility together.

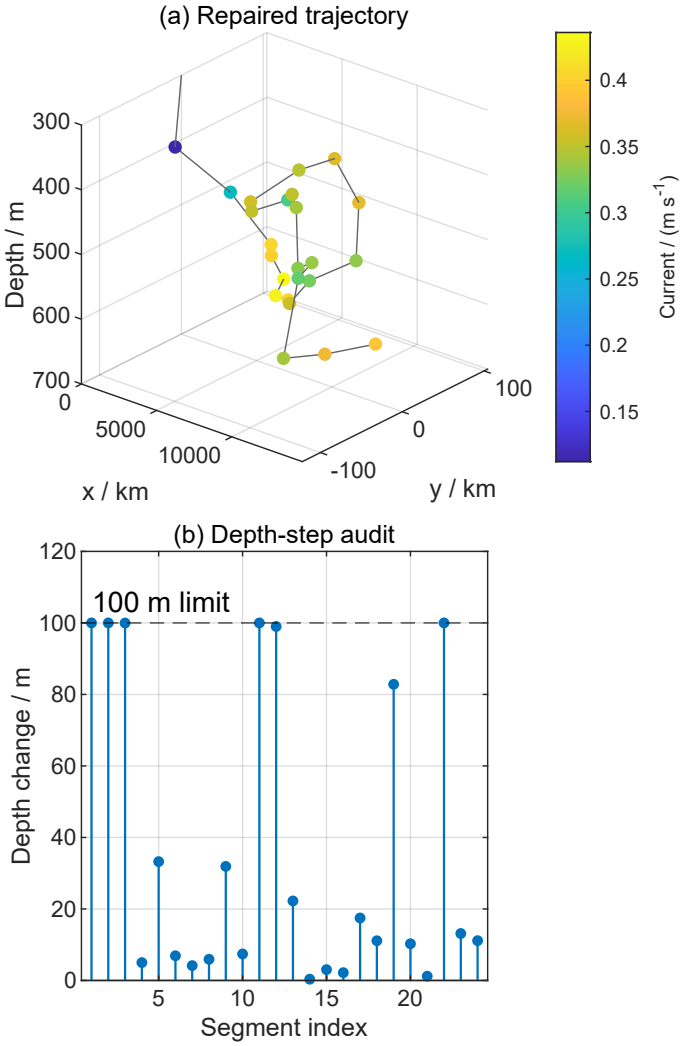


Figure 4. Case E: (a) three-dimensional segment-wise trajectory, colored by local current; (b) absolute depth changes, including the first transition from 300 m, relative to the 100 m limit.

6.4 Conditions Affecting Depth Optimization

To determine whether depth adjustment benefits from vertical environmental variation and to assess its interaction with energy-system limits, Cases D and E were evaluated under five paired conditions (Table 6). In these tests, the vertical amplitude of the favorable-current depth center along the track was set to $A_z = 0$, 170, and 340 m; the Gaussian depth dependence was retained in all three cases. In power-system tests, the nominal fuel cell range

Table 5. Constraint values of the representative Case E solution. The numerical tolerance is 10^{-8}; the fuel cell power-step quantity is reported as a command-sequence metric.

Constraint	Evaluated value and prescribed requirement	Positive residual
Speed bounds	1.647–2.117 m/s; required 1.0–2.5 m/s	0 m/s
Depth bounds	365.806–649.267 m; search interval 150–900 m, physical interval 100–1000 m	0 m
Horizontal turning	Maximum 18.225 degrees; limit 30 degrees	0 degrees
Adjacent depth change	Maximum 100.000 m; limit 100 m, including initial-depth transition	0 m
Mission duration	2215.513 h; declared audit limit 2230.096 h	0 h
Fuel cell output	Actual minimum 160.000 kW; all values within 160–640 kW	0 kW
SOC lower/upper bounds	Minimum 0.344527, maximum 0.850000; required 0.20–0.85	$\leq 10^{-8}$
Terminal SOC recovery	Deviation 0.025286; limit 0.03	0
Fuel cell step change	Maximum 96.480 kW; no independent ramp limit specified	Not applicable

Table 6. Paired sensitivity of Cases D and E to vertical-current structure and energy-system limits. Each condition uses ten paired seeds. Δ is the relative change in mean hydrogen consumption for E versus D; negative values favor E.

Condition	Feasible D/E	Mean H_2 / kg D/E	Δ (%)	RSD D/E (%)	E lower (paired runs)
$A_z = 0$ m; nominal power	10/10	26214.35 / 26102.75	-0.43	0.000 / 16.643	8/10
$A_z = 170$ m; nominal power	10/10	26104.61 / 23190.76	-11.16	0.068 / 3.022	10/10
$A_z = 340$ m; nominal power	10/10	26706.57 / 25120.94	-5.94	0.102 / 1.351	10/10
$A_z = 170$ m; fuel cell 220–520 kW	10/10	30295.26 / 31125.43	$+2.74$	3.616 / 6.468	4/10
$A_z = 170$ m; battery 4 MWh	10/10	26112.12 / 23809.68	-8.82	0.000 / 4.676	9/10

and battery capacity (160–640 kW and 8 MWh) were compared with a narrower fuel cell range (220–520 kW) and a reduced battery capacity (4 MWh).

For the nominal power system, Case E reduces mean hydrogen consumption by 11.16% at $A_z = 170$ m and 5.94% at $A_z = 340$ m; all ten paired runs favor E in both conditions. Without along-track vertical variation ($A_z = 0$ m), the mean advantage shrinks to 0.43%, only 8/10 paired runs favor E, and the RSD of Case E rises to 16.6%. Narrowing the fuel cell range to 220–520 kW reverses the sign ($+2.74\%$, 4/10), whereas halving the battery capacity to 4 MWh still leaves an 8.82% advantage (9/10).

6.5 Algorithm Baseline and Component Ablation

To assess whether the reported performance depends on the PSO search mechanism and the proposed initialization and feasibility-handling components, a focused algorithmic comparison was conducted under a matched budget. All configurations use the Case E decision space, the same physical model, bounds, depth repair when enabled, feasibility audit, 50 particles or individuals, 120 generations, and ten random seeds. Thus, each run receives 6000 objective evaluations. Differential evolution (DE) is used as a representative non-PSO metaheuristic.

Under the matched budget (Table 7), PSO obtains a higher feasibility rate and lower hydrogen consumption than DE. For the nine paired feasible runs, the mean DE–PSO difference is 9587.61 kg, with a 95% paired confidence interval of [8144.29, 11030.93] kg and an exact two-sided sign-permutation p-value of 0.003906. This comparison supports the suitability of the PSO-based search for the present constrained model under the tested budget.

Table 8 shows that the speed prior matters most: without it, only seven runs are feasible and mean consumption rises by 26.6%. Removing the lateral prior, the depth prior, or depth repair raises mean

Table 7. Separate matched-budget algorithm batch for Case E: 50 particles or individuals, 120 generations, 6000 evaluations, and ten common seeds. Values are distinct from the main Table 4 batch.

Method	Feasible /10	Mean H_2 / kg	SD / kg	RSD / %	Median first feasible evaluation	Median evaluation to 90%
PSO	10	23157.67	357.83	1.545	132	4604.5
DE	9	32744.41	2089.65	6.382	2576	4307.0

Table 8. Component ablations from the same matched-budget batch as Table 7: 50 particles, 120 generations, 6000 evaluations, and ten common seeds.

Configuration	Feasible /10	Mean H_2 / kg	RSD / %	Median first feasible evaluation	Mean depth violation / m
Full PSO configuration	10	23157.67	1.545	132	0.000
Without speed prior	7	29322.80	13.201	2657	0.000
Without lateral prior	10	26933.41	5.242	415	0.000
Without depth prior	10	25390.03	3.694	1	0.000
Without depth repair	9	26285.15	7.131	2861	0.503
Without feasibility-first selection	10	23006.66	1.864	132	0.000

Table 9. Sensitivity of Cases D and E to propulsion-load model parameters. Each condition uses ten paired seeds; all runs are fully feasible. CI denotes the paired 95% confidence interval of $m_{\mathrm{H}_2,E} - m_{\mathrm{H}_2,D}$.

Condition	Mean H_2 / kg D/E	E vs. D / %	Paired CI / kg	E lower / 10
Nominal	26104.61 / 23190.76	-11.16	$[-3420.31, -2407.40]$	10
Combined coefficient -10%	25227.39 / 23455.33	-7.02	$[-3129.34, -414.78]$	9
Combined coefficient $+10\%$	27873.86 / 25080.17	-10.02	$[-3331.22, -2256.15]$	10
Depth-maneuver multiplier -50%	26104.61 / 22468.27	-13.93	$[-4307.81, -2964.86]$	10
Depth-maneuver multiplier $+50\%$	26104.61 / 25069.77	-3.96	$[-2648.29, 578.60]$	8
Turning multiplier -50%	25759.17 / 22660.85	-12.03	$[-3431.37, -2765.27]$	10
Turning multiplier $+50\%$	26452.02 / 23342.10	-11.76	$[-3419.64, -2800.21]$	10
Depth-operating slope -10%	26104.61 / 23192.41	-11.16	$[-3331.10, -2493.29]$	10
Depth-operating slope $+10\%$	26104.61 / 23406.41	-10.34	$[-2935.58, -2460.82]$	10

consumption by 16.3%, 9.6%, and 13.5%, respectively, and without depth repair one run is infeasible and the mean depth-step violation becomes 0.503 m. Removing feasibility-first selection does not worsen the objective in this batch (23006.66 versus 23157.67 kg, with a slightly higher RSD); its role here is to keep feasible incumbents rather than to lower hydrogen use.

6.6 Sensitivity to Propulsion-Load Parameters

To quantify the dependence of the depth-related result on the simplified propulsion-load representation, Cases D and E were reoptimized under one-at-a-time perturbations using the same ten paired seeds and the full feasibility audit. The combined resistance–propulsion coefficient was varied by $\pm 10\%$; the depth-maneuver load multiplier and turning load multiplier were varied by $\pm 50\%$. A further $\pm 10\%$ depth-operating slope was applied to the combined propulsion coefficient as a proxy for depth-dependent propulsion efficiency, because the nominal model does not independently identify $C_D(z)$ and $\eta_p(z)$. Table 9 summarizes the perturbations; the reported percentage is the relative change in mean hydrogen consumption for E versus D.

Table 10. Sensitivity of lateral trajectory optimization to ocean-current structure. Saving is the reduction in mean hydrogen consumption for Case D relative to Case B.

Current-field condition	Mean H_2 / kg B/D	Mean saving / %	Saving range / %	D lower
Nominal	27725.13 / 26104.61	5.84	5.62–6.04	10/10
Corridor offset -60 km	29108.68 / 26762.35	8.06	8.03–8.15	10/10
Corridor offset $+60$ km	29153.85 / 25348.74	12.70	8.22–25.04	10/10
Lateral decay scale 50 km	29441.74 / 26107.07	11.33	11.05–11.62	10/10
Lateral decay scale 100 km	26876.86 / 26102.45	2.88	2.61–2.95	10/10
Current direction -15°	27806.23 / 26239.47	5.63	5.44–5.82	10/10
Current direction $+15^\circ$	27806.23 / 26272.92	5.51	5.31–5.79	10/10
20 randomized fields	—	6.38 ± 2.90	2.77–15.49	20/20

Table 11. Energy-system and propulsion-load parameters used in the simulation.

Quantity	Symbol or model	Nominal value	Basis/source
Fuel cell rated and operating power	P_{rated}; $[P_{\mathrm{fc,min}}, P_{\mathrm{fc,max}}]$	800 kW; [160, 640] kW	Mission-level system design assumption
Fuel cell efficiency	$\eta_{\mathrm{fc}}(P_{\mathrm{fc}})$	Parametric curve in (21)	Mission-level parametric model; sensitivity tested
Hydrogen lower heating value	$\mathrm{LHV}_{\mathrm{H_2}}$	33.5 kWh kg^{-1}	Lower-heating-value assumption (approx. 120 MJ kg^{-1})
Nominal battery energy capacity	E_{bat}	8 MWh = 8000 kWh	Mission-level system design assumption
Charge/discharge efficiency	$\eta_{\mathrm{ch}}/\eta_{\mathrm{dis}}$	0.92 / 0.94	Mission-level system design assumption
SOC settings	SOC_0; $[SOC_{\min}, SOC_{\max}]$	0.60; [0.20, 0.85]	Prescribed operating constraints
Terminal SOC recovery	$\lvert SOC_N - SOC_0 \rvert$	≤ 0.03	Prescribed mission constraint
SOC feedback gain	k_{SOC}	240 kW per unit SOC	Implemented power-allocation parameter
Fuel cell bias decision	$\delta P_{\mathrm{fc},i} = 18\epsilon_i$, $\epsilon_i \in [-1, 1]$	$[-18, 18]$ kW	Optimized segment-wise decision variable
Auxiliary load	P_{aux}	62 kW	Mission-level load assumption
Effective resistance–propulsion coefficient	κ_{prop}	27.5 kW/(m s^{-1})^3	Combined coefficient; sensitivity tested
Turning/depth load multipliers	k_ψ/k_z	0.018 degree^{-1} / 0.004 m^{-1}	Implemented maneuver-load parameters; sensitivity tested
Fuel cell command step	$\Delta P_{\mathrm{fc},i}$	Diagnostic; no prescribed limit	Calculated from adjacent segment commands

Across these perturbations, all 180 solutions remain feasible and the mean Case E consumption remains below Case D by 3.96–13.93%. The largest variability occurs for the positive depth-maneuver perturbation, where the paired interval includes zero; this changes the strength of the observed benefit while preserving solution feasibility.

6.7 Sensitivity to Ocean-Current Structure

The influence of the current-field geometry on lateral trajectory optimization was evaluated by comparing Case D with the fixed-route speed–power Case B. One-at-a-time tests varied the favorable-corridor lateral offset by ± 60 km, its Gaussian lateral decay scale from the nominal 75 km to 50 and 100 km,

Table 12. Case E energy-parameter batch with ten common seeds and 50 particles × 120 generations per condition. The nominal row is internal to this batch and distinct from Tables 4, 7, and 8. S_{fc} is averaged across the ten trials. FC denotes fuel cell.

Condition	Mean H_2 / kg	Change / %	Final SOC	E_{thr} / MWh	Mean S_{fc} / kW
Nominal	23131.31	0.00	0.587	35.80	757.82
FC efficiency scale -5%	24348.75	$+5.26$	0.587	35.80	757.82
FC efficiency scale $+5\%$	22029.82	-4.76	0.587	35.80	757.82
$\eta_{\mathrm{ch}}/\eta_{\mathrm{dis}} = 0.89/0.91$	21837.31	-5.59	0.585	8.76	262.23
$\eta_{\mathrm{ch}}/\eta_{\mathrm{dis}} = 0.95/0.97$	22965.71	-0.72	0.588	32.67	817.94
Initial SOC 0.55	23278.05	$+0.63$	0.535	36.33	773.34
Initial SOC 0.65	22673.15	-1.98	0.637	23.76	616.90
Terminal tolerance ± 0.02	24039.89	$+3.93$	0.597	34.97	1068.66
Terminal tolerance ± 0.04	22935.45	-0.85	0.576	25.45	705.48
Auxiliary load -10%	22855.75	-1.19	0.597	41.99	755.60
Auxiliary load $+10\%$	24096.79	$+4.17$	0.586	31.35	1021.31

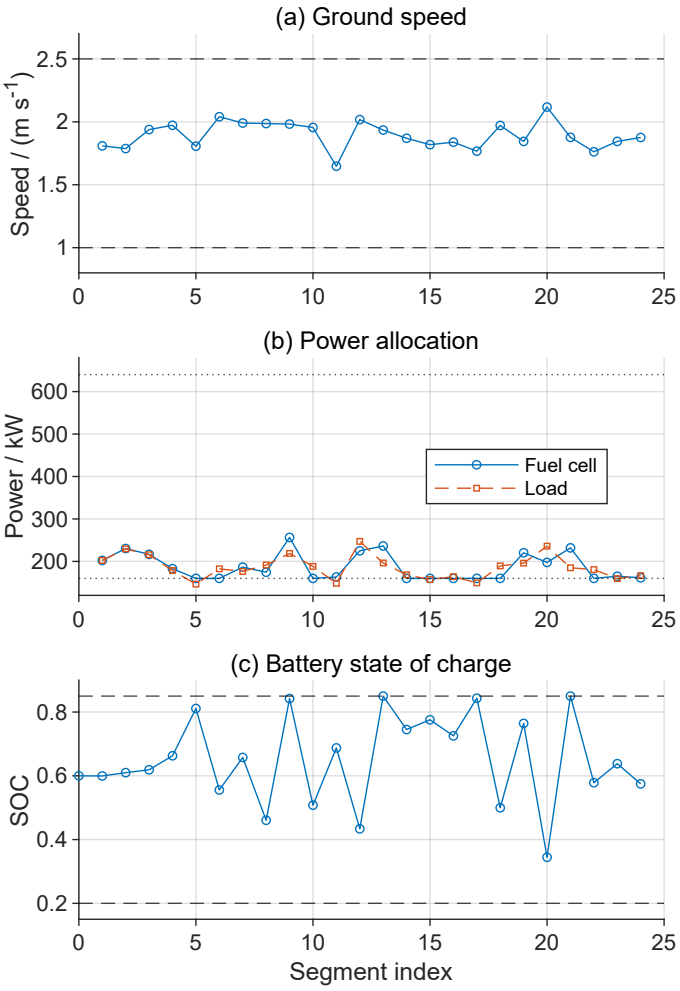


Figure 5. Case E: (a) ground speed; (b) fuel cell output and load demand; (c) SOC at segment ends, including the initial value. Dashed lines mark prescribed limits.

and the horizontal current direction by $\pm 15°$. Each condition used ten paired solver seeds. In addition, 20 randomized fields jointly sampled the corridor offset from $[-60, 60]$ km, decay scale from $[50, 100]$ km, along-track phase from $[-\pi/4, \pi/4]$, and current direction from $[-15°, 15°]$. A common solver seed was used across the randomized fields so that their distribution reflects environmental variation rather than optimizer-seed variation.

All 140 solutions in the one-at-a-time tests (Table 10) are feasible, and Case D has lower hydrogen consumption in every paired run. Across the 20 randomized fields, all Case B/D pairs are feasible and the lateral-optimization saving is positive in every field, with a mean of 6.38%, a standard deviation of 2.90%, and a range of 2.77–15.49%. The variation in saving magnitude confirms that the benefit depends on current-field structure, while the tested fields retain a consistent advantage from lateral trajectory freedom.

6.8 Energy-System Parameters and Sensitivity

Table 11 consolidates the parameters used in the energy-system and propulsion-load calculations. Platform-specific quantities that are not taken from measured prototype data are identified as mission-level design assumptions, while the hydrogen lower heating value is a standard physical property. The nominal fuel cell efficiency curve is

$$\eta_{\mathrm{fc}}(r) = \mathrm{clip}_{[0.35,0.60]}\left[0.545 - 0.16(r - 0.52)^2\right], \quad r = P_{\mathrm{fc}}/P_{\mathrm{rated}}. \tag{21}$$

Case E was reoptimized under one-at-a-time variations of the fuel cell efficiency curve ($\pm 5\%$), battery charge/discharge efficiencies (0.89/0.91 and 0.95/0.97), initial SOC (0.55 and 0.65), terminal SOC tolerance (± 0.02 and ± 0.04), and auxiliary load ($\pm 10\%$). Each

condition used ten independent seeds and the same full feasibility audit. Table 12 reports the feasible-run means; its nominal row belongs to this separate sensitivity batch and is the reference for the reported percentage changes.

All 110 sensitivity runs satisfy the complete constraint set. Mean hydrogen consumption changes by -5.59% to $+5.26\%$ relative to the sensitivity-batch nominal value. The fuel cell curve directly scales hydrogen use, while the SOC, battery-efficiency, and auxiliary-load perturbations also change the selected battery throughput and fuel cell command sequence. The battery-efficiency response is not monotonic: the lower-efficiency setting gives the lowest mean consumption and coincides with a much smaller battery throughput (8.76 versus 35.80 MWh), which points to a different search outcome under the fixed budget rather than a physical benefit of lower efficiency. The stricter terminal recovery tolerance increases mean hydrogen consumption by 3.93%, and the 10% auxiliary-load increase raises it by 4.17%.

7 Conclusion

A mission-level trajectory–speed–energy three-dimensional optimization framework is developed for XLUUVs by jointly encoding lateral trajectory positions, segment depths and speeds, and fuel cell biases. The solver combines a composite prior-guided seed, explicit sequential depth repair, hierarchical power/SOC projection, and feasibility-first PSO selection for the coupled operational constraints.

Under the nominal analytical-current scenario, all Case E runs satisfy the complete discrete constraint set and achieve a mean hydrogen consumption of 23190.76 kg, corresponding to a 30.34% saving relative to Case A and an 11.16% reduction relative to Case D. The sensitivity studies show that these gains are conditional: depth freedom provides little evidence of benefit without along-track vertical-current variation and becomes unfavorable when the fuel cell range is narrowed, whereas lateral trajectory freedom remains beneficial across the tested randomized current fields. Case F achieves a 32.19% saving and outperforms Case E under the adopted model and budget, indicating that unified formulation alone does not guarantee the best numerical solution. The reported figures hold for the specified mission model, current fields, energy-system limits, propulsion parameterization, and optimization budget. Future work will replace the simplified propulsion and analytical-current representations with computational fluid dynamics (CFD) or measured hydrodynamic data and depth-resolved ocean reanalysis.

Data Availability Statement

The data used to support the findings of this study are available from the corresponding author upon request.

Funding

This work was supported by the National Natural Science Foundation of China under Grant 20241380002.

Conflicts of Interest

The authors declare no conflicts of interest.

AI Use Statement

The authors declare that no generative AI was used in the preparation of this manuscript.

Ethical Approval and Consent to Participate

Not applicable.

References

[1] Button, R. W., Kamp, J., Curtin, T. B., & Dryden, J. (2009). *A Survey of Missions for Unmanned Undersea Vehicles* (MG-808-NAVY). RAND Corporation, Santa Monica, CA. https://www.rand.org/pubs/monographs/MG808.html

[2] O'Rourke, R. (2025). *Navy Large Unmanned Surface and Undersea Vehicles: Background and Issues for Congress* (CRS Report No. R45757). Congressional Research Service, Washington, DC. https://www.congress.gov/crs-product/R45757

[3] Sahoo, A., Dwivedy, S. K., & Robi, P. S. (2019). Advancements in the Field of Autonomous Underwater Vehicle. *Ocean Engineering, 181*, 145–160. [CrossRef]

[4] Lin, Z., Qin, D., Huang, Q., Dong, H., & Pan, G. (2026). Review of Energy Technologies for Unmanned Underwater Vehicles. *Energies, 19*(3), 592. [CrossRef]

[5] Liu, S., Wang, Z., Wang, T., Zhou, S., Zhang, Y., Jin, P., & Yang, G. (2025). Energy-Optimized Path Planning for Fully Actuated AUVs in Complex 3D Environments. *Journal of Marine Science and Engineering, 13*(7), 1269. [CrossRef]

[6] Wang, X., Shang, J., Luo, Z., Tang, L., Zhang, X., & Li, J. (2012). Reviews of Power Systems and Environmental Energy Conversion for Unmanned Underwater Vehicles. *Renewable and Sustainable Energy Reviews, 16*(4), 1958–1970. [CrossRef]

[7] Chiche, A., Lindbergh, G., Stenius, I., & Lagergren, C. (2021). A Strategy for Sizing and Optimizing the Energy System on Long-Range AUVs. *IEEE Journal of Oceanic Engineering, 46*(4), 1132–1143. [CrossRef]

[8] Deutsch, C., Chiche, A., Bhat, S., Lagergren, C., Lindbergh, G., & Kuttenkeuler, J. (2022). Evaluation of Energy Management Strategies for Fuel Cell/Battery-Powered Underwater Vehicles Against Field Trial Data. *Energy Conversion and Management: X, 14*, 100193. [CrossRef]

[9] Mendez, A., Leo, T. J., & Herreros, M. A. (2014). Current State of Technology of Fuel Cell Power Systems for Autonomous Underwater Vehicles. *Energies, 7*(7), 4676–4693. [CrossRef]

[10] Psaraftis, H. N., & Kontovas, C. A. (2014). Ship Speed Optimization: Concepts, Models and Combined Speed-Routing Scenarios. *Transportation Research Part C: Emerging Technologies, 44*, 52–69. [CrossRef]

[11] Barreiro, J., Zaragoza, S., & Diaz-Casas, V. (2022). Review of Ship Energy Efficiency. *Ocean Engineering, 257*, 111594. [CrossRef]

[12] Fan, A. L., Yang, J., Yang, L., Liu, W. Q., & Vladimir, N. (2022). Joint Optimisation for Improving Ship Energy Efficiency Considering Speed and Trim Control. *Transportation Research Part D: Transport and Environment, 113*, 103527. [CrossRef]

[13] Li, X. H., Sun, B. Z., Jin, J. H., & Ding, J. (2022). Speed Optimization of Container Ship Considering Route Segmentation and Weather Data Loading: Turning Point-Time Segmentation Method. *Journal of Marine Science and Engineering, 10*(12), 1835. [CrossRef]

[14] Yuan, Y. P., Wang, X. Y., Tong, L., Yang, R., & Shen, B. Y. (2023). Research on Multi-Objective Energy Efficiency Optimization Method of Ships Considering Carbon Tax. *Journal of Marine Science and Engineering, 11*(1), 82. [CrossRef]

[15] Wang, N., & Li, Z. Q. (2025). PSO-Based Speed and Power Allocation Strategy Collaborative Optimization Method for Hydrogen Fuel Cell Ships. *Chinese Journal of Ship Research, 20*(3), 211–222 (in Chinese). [CrossRef]

[16] Yan, X., Wang, K., Yuan, Y., Jiang, X., & Negenborn, R. R. (2018). Energy-efficient shipping: An application of big data analysis for optimizing engine speed of inland ships considering multiple environmental factors. *Ocean Engineering, 169*, 457-468. [CrossRef]

[17] Petres, C., Pailhas, Y., Petillot, Y., & Lane, D. (2005, June). Underwater path planing using fast marching algorithms. In *Europe Oceans 2005* (Vol. 2, pp. 814-819). IEEE. [CrossRef]

[18] Garau, B., Alvarez, A., & Oliver, G. (2005). Path Planning of Autonomous Underwater Vehicles in Current Fields with Complex Spatial Variability: An A* Approach. In *Proceedings of the 2005 IEEE International Conference on Robotics and Automation* (pp. 194–198). IEEE, Barcelona, Spain. [CrossRef]

[19] Alvarez, A., Caiti, A., & Onken, R. (2004). Evolutionary Path Planning for Autonomous Underwater Vehicles in a Variable Ocean. *IEEE Journal of Oceanic Engineering, 29*(2), 418–429. [CrossRef]

[20] Witt, J., & Dunbabin, M. (2008). Go with the Flow: Optimal AUV Path Planning in Coastal Environments. In *Proceedings of the Australasian Conference on Robotics and Automation* (*ACRA 2008*). https://www.araa.asn.au/acra/acra2008/papers/pap133s1.pdf

[21] Alam, T., Al Redwan Newaz, A., Bobadilla, L., Alsabban, W. H., Smith, R. N., & Karimoddini, A. (2021). Towards energy-aware feedback planning for long-range autonomous underwater vehicles. *Frontiers in Robotics and AI, 8*, 621820. [CrossRef]

[22] Tang, D., & Wang, H. (2021). Energy management strategies for hybrid power systems considering dynamic characteristics of power sources. *IEEE Access, 9*, 158796-158807. [CrossRef]

[23] Zhou, S., Fan, L., Zhang, G., Gao, J., Lu, Y., Zhao, P., Wen, C., Shi, L., & Hu, Z. (2022). A Review on Proton Exchange Membrane Multi-Stack Fuel Cell Systems: Architecture, Performance, and Power Management. *Applied Energy, 310*, 118555. [CrossRef]

[24] Mutarraf, M. U., Terriche, Y., Niazi, K. A. K., Vasquez, J. C., & Guerrero, J. M. (2018). Energy Storage Systems for Shipboard Microgrids—A Review. *Energies, 11*(12), 3492. [CrossRef]

[25] Hou, J., Sun, J., & Hofmann, H. (2018). Control Development and Performance Evaluation for Battery/Flywheel Hybrid Energy Storage Solutions to Mitigate Load Fluctuations in All-Electric Ship Propulsion Systems. *Applied Energy, 212*, 919–930. [CrossRef]

[26] Wang, X. Y., Zhu, J. Z., & Han, M. F. (2023). Industrial Development Status and Prospects of the Marine Fuel Cell: A Review. *Journal of Marine Science and Engineering, 11*(2), 238. [CrossRef]

[27] Song, K., Ding, Y. H., Hu, X., Xu, H. J., Wang, Y. M., & Cao, J. (2021). Degradation Adaptive Energy Management Strategy Using Fuel Cell State-of-Health for Fuel Economy Improvement of Hybrid Electric Vehicle. *Applied Energy, 285*, 116413. [CrossRef]

[28] Fossen, T. I. (2021). *Handbook of Marine Craft Hydrodynamics and Motion Control* (2nd ed.). Wiley, Chichester. [CrossRef]

[29] Groves, N. C., Huang, T. T., & Chang, M. S. (1989). *Geometric Characteristics of DARPA SUBOFF Models* (Report DTRC/SHD-1298-01). David Taylor Research Center, Bethesda. https://www.scribd.com/document/105661195/Geometry-Darpa-Models

[30] Liu, H. L., & Huang, T. T. (1998). *Summary of DARPA SUBOFF Experimental Program Data* (Report CRDKNSWC/HD-1298-11). Naval Surface Warfare Center, Carderock Division, Bethesda. https://scispace.com/pdf/summary-of-darpa-suboff-experimental-program-data-29apxlb3tz.pdf

[31] Kennedy, J., & Eberhart, R. (1995, November). Particle swarm optimization. In *Proceedings of ICNN'95 - International Conference on Neural Networks* (Vol. 4, pp. 1942-1948). IEEE. [CrossRef]

[32] Clerc, M., & Kennedy, J. (2002). The particle swarm-explosion, stability, and convergence in a multidimensional complex space. *IEEE Transactions on Evolutionary Computation*, *6*(1), 58-73. [CrossRef]



Peng Bo received the Ph.D. degree in Marine Technology and Engineering from Zhejiang University in 2024. He is currently a Postdoctoral Researcher with the Department of Mechanical Engineering, Tsinghua University, Beijing, China. His research interests include the filtering and control of autonomous marine vehicles, and the design of communication and control protocols for distributed unmanned marine platforms.



Qingchang Guo received the B.E. degree in Thermal Energy and Power Engineering from Harbin Engineering University in 2003 and the Ph.D. degree in Pattern Recognition and Intelligent Systems from Harbin Engineering University in 2008. He is currently a Researcher at Tsinghua University, Beijing, China. His research interests include the overall design of unmanned underwater platforms.



Liran Ma received the B.E. degree from Tsinghua University in 2005 and the Ph.D. degree from Tsinghua University in 2010. She is currently a Professor at Tsinghua University, Beijing, China. Her research interests include tribology, interface science and technology, superlubricity, drag and noise reduction, and underwater equipment.



Jianbin Luo received the B.Eng. degree in Metalworking from Northeastern University, China, in 1982, the M.Eng. degree in Metalworking from Xi'an University of Architecture and Technology in 1988, and the Ph.D. degree in Mechanical Design and Theory from Tsinghua University, Beijing, China, in 1994. He joined the faculty of Tsinghua University in 1994 and is currently a Professor there. He is an Academician of the Chinese Academy of Sciences and a Fellow of The World Academy of Sciences (TWAS). He previously served as the Dean of the School of Mechanical Engineering at Tsinghua University. His research interests include superlubricity, thin-film lubrication, and nanomanufacturing. He is the Editor-in-Chief of the English-language journal Friction. He has received numerous awards, including the Tan Kah Kee Science Award in Technological Sciences in 2020, the STLE International Award, and the CTI Highest Achievement Award in Tribology in 2013. He has published more than 700 papers and two books, and holds more than 200 authorized patents.